PHYSICAL REVIEW B **94**, 094404 (2016)

Superharmonic injection locking of nanocontact spin-torque vortex oscillators

P. S. Keatley,[1,*] S. R. Sani,[2,3,4] G. Hrkac,[5] S. M. Mohseni,[6] P. Dürrenfeld,[7] J. Åkerman,[2,3,7] and R. J. Hicken[1]
[1]*Department of Physics and Astronomy, University of Exeter, Stocker Road, Exeter, EX4 4QL, United Kingdom*
[2]*Materials and Nano Physics, School of ICT, KTH Royal Institute of Technology, Electrum 229, 164 40 Kista, Sweden*
[3]*NanOsc AB, Electrum 205, 164 40 Kista, Sweden*
[4]*Department of Physics & Astronomy, Uppsala University, Box 516, SE-751 20 Uppsala, Sweden*
[5]*College of Engineering, Mathematics and Physical Science, University of Exeter, Exeter, EX4 4SB, United Kingdom*
[6]*Department of Physics, Shahid Beheshti University, G.C., Evin, Tehran 19839, Iran*
[7]*Physics Department, University of Gothenburg, Fysikgränd 3, 412 96 Gothenburg, Sweden*

(Received 6 April 2016; published 6 September 2016)

Superharmonic injection locking of single nanocontact (NC) spin-torque vortex oscillators (STVOs) subject to a small microwave current has been explored. Frequency locking was observed up to the fourth harmonic of the STVO fundamental frequency f_0 in microwave magnetoelectronic measurements. The large frequency tunability of the STVO with respect to f_0 allowed the device to be locked to multiple subharmonics of the microwave frequency f_{RF}, or to the same subharmonic over a wide range of f_{RF} by tuning the dc current. In general, analysis of the locking range, linewidth, and amplitude showed that the locking efficiency decreased as the harmonic number increased, as expected for harmonic synchronization of a nonlinear oscillator. Time-resolved scanning Kerr microscopy (TRSKM) revealed significant differences in the spatial character of the magnetization dynamics of states locked to the fundamental and harmonic frequencies, suggesting significant differences in the vortex core trajectories within the same device. Superharmonic injection locking of a NC-STVO may open up possibilities for devices such as nanoscale frequency dividers, while differences in the core trajectory may allow mutual synchronization to be achieved in multioscillator networks by tuning the spatial character of the dynamics within shared magnetic layers.

DOI: 10.1103/PhysRevB.94.094404

I. INTRODUCTION

Since the prediction [1,2] and realization [3,4] of spin transfer torque (STT) there have been significant advances in order to utilize the effect in nanoscale nonlinear microwave oscillators [5,6]. In such a device STT acts to counteract and balance the magnetic damping of a ferromagnetic resonance [7] allowing for autonomous (auto-) oscillations of the magnetization to be realized [8,9]. These so-called spin-torque oscillators (STOs) are attractive for nanoscale STO-based devices such as broadband microwave generators owing to their high frequency tunability (100 MHz to 100 GHz) [10,11]. The microwave emission of STOs can be generated by gigahertz magnetization precession [8] or megahertz vortex gyration [10,12] depending on the applied magnetic field [13]. In contrast to precession-based STOs, vortex oscillators exhibit multioctave frequency tenability [14] and relatively high output power [13], resulting in significant interest from applied and fundamental perspectives. While the output power of vortex auto-oscillations can be more than two orders of magnitude larger than precession-based oscillations in the same device [13], the output power remains too low for technological applications [6]. At the same time, it is recognized that the linewidth of STOs can be undesirably large, owing to the frequency and phase noise of the auto-oscillations [15–20]. This has led to a number of studies of the mutual synchronization of multiple STOs [13,21–30] and phase locking of STOs to an injected microwave (RF) current [20,31–36] in an attempt to enhance their output power and phase stability.

The synchronization and locking of STOs depends upon their nonlinear nature [37]. In this work the nonlinear character is utilized to achieve superharmonic injection locking (SHIL) of a nanocontact (NC) spin-torque vortex oscillator (STVO) subject to an injected RF current with a frequency f_{RF} that corresponds to higher harmonics (nf_0) of the fundamental STVO auto-oscillation frequency f_0. SHIL is observed up to the fourth harmonic ($4f_0$) in microwave magnetoelectronic measurements, while time-resolved scanning Kerr microscopy (TRSKM) is used to observe differences in the spatial character of magnetization dynamics generated by the STVO when injection locked to either its fundamental frequency f_0, or the second harmonic frequency ($2f_0$) through SHIL. Previously, SHIL has been used in complimentary metal-oxide-semiconductor (CMOS) technology to construct an injection-locked frequency divider (ILFD) that produces a phase-locked response at a fraction of the applied microwave signal [38,39]. The multioctave tunability of the STVO allows SHIL to be observed at multiple subharmonics (e.g., $f_{\mathrm{RF}}/2$ and $f_{\mathrm{RF}}/3$) for a particular frequency of the injected RF current. Hence, this work demonstrates that STVOs may also find a potential application as nanoscale ILFDs that utilize SHIL.

Recently, SHIL in a STVO was demonstrated in a single magnetic tunnel valve nanopillar geometry consisting of a double vortex configuration of the free and reference layers [20]. In a nanopillar STVO the magnetization dynamics are confined by the physical boundaries of the pillar. In contrast, here we demonstrate SHIL in a nanocontact (NC) geometry in which the applied current was confined by the NC before entering an extended spin valve film. Our aims are to

---

[*] Corresponding author: p.s.keatley@exeter.ac.uk

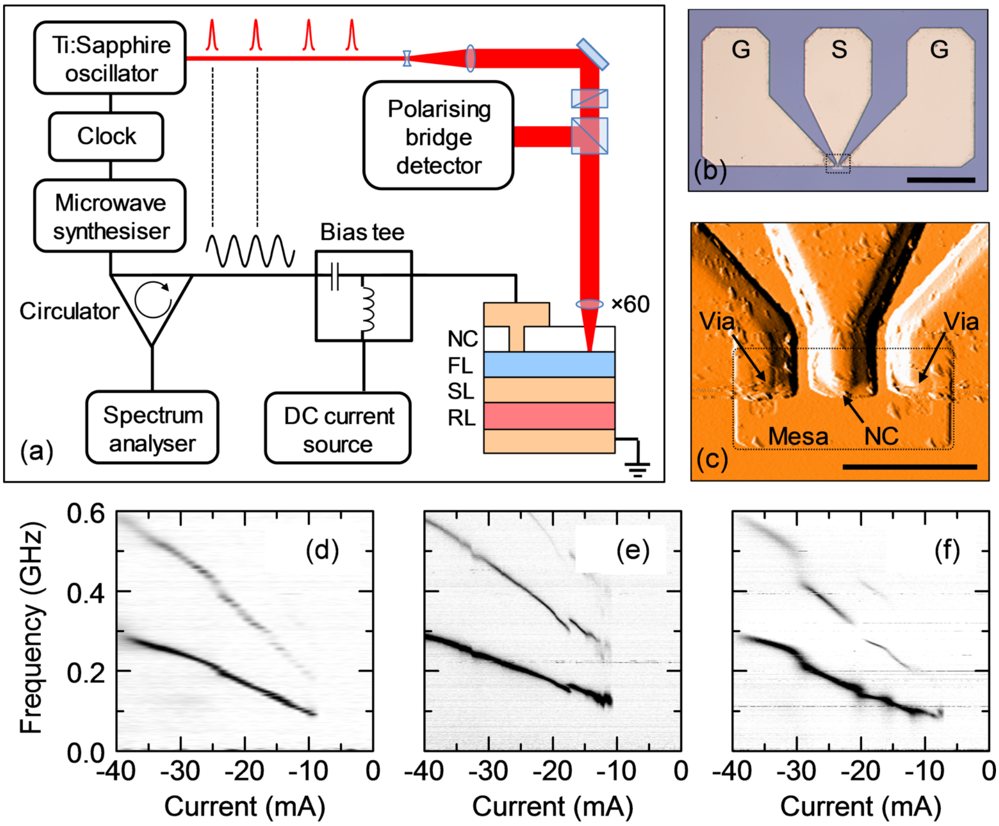

FIG. 1. (a) Experimental setup of combined magnetoelectronic measurements and TRSKM with coherent injection locking. (b) An optical microscope image of the CPW geometry of the ground (G) and signal (S) electrical contact pads (scale bar 100 μm). (c) A contact mode atomic force microscope image of the contact pad geometry on top of the spin valve mesa (dotted rectangle) that allows optical access to approximately half of the mesa (scale bar 10 μm). The location of the vias and the approximate location of the NC are indicated by arrows. In (d), (e), and (f) the STVO signal as a function of dc current only is shown for three single NC devices (NC1, NC2, and NC3, respectively) all with a nominal NC diameter of 250 nm. In (d)–(f) white and black correspond to 0 and 1 nV/Hz$^{1/2}$, respectively.

(i) understand the electrical character of a NC-STVO when locked to fractions of an injected RF current, (ii) understand how the spatial character of the free layer magnetization dynamics is associated with the fraction at which the NC-STVO is locked, even if the locked frequency is the same, and (iii) to discuss how the vortex oscillator may be locked through interaction with an Oe field that is modulated at the RF frequency.

II. EXPERIMENTAL SETUP AND SAMPLE DETAILS

In this study each STVO was formed from a single metallic NC fabricated on top of a microscale spin valve mesa. The nominal diameter of the NCs was 250 nm. A spin valve multilayer film, consisting of Pd(8)/Cu(15)/Co(8)/Cu(7)/$Ni_{81}Fe_{19}$(4.5)/Cu(3)/Pd(3) (thickness in nanometers), was deposited onto a Si/SiO_2 (thermally oxidized, 1 μm) substrate using magnetron sputtering in an argon plasma from a base pressure of $<2 \times 10^{-8}$ Torr. Photolithography and argon dry etching were then used to define a spin valve mesa with lateral size of $16 \times 8\,\mu m^2$. The Co, Cu(7), and NiFe layers formed the reference (RL), spacer (SL), and free layers (FL) of the spin valve, respectively, Fig. 1(a). The bottom Cu(15) layer ensured that a significant proportion of the current passing through the NC flowed perpendicular to the magnetic layers to provide sufficient STT for device functionality, where a positive current represents electrons moving from the RL to the FL. To fabricate the NC, a SiO_2(30) layer was first deposited on top of the mesa using plasma enhanced chemical vapor deposition. The NC was then defined using electron-beam lithography, followed by reactive ion etching.

A coplanar waveguide (CPW), designed with a characteristic impedance of 50 Ω, was used to make electrical contacts to the NC, Fig. 1(b). The CPW was formed using a sputtered Cu(1200)/Au(20) bilayer and a lift-off technique, and was specifically designed to only cover approximately half of the spin valve mesa allowing for optical access to the exposed FL (capped with SiO_2), Fig. 1(c) (cf. CPW design in Ref. [13]). The NC was located at the center of the mesa, which approximately places it on the symmetry axis and close to the edge of the center contact pad [see arrow in Fig. 1(c)]. The thick Cu contact pad provided an effective heat sink for device operation up to a current density of $\sim 2 \times 10^8$ A/cm^2, while the Au cap allowed for good electrical contact to the external electronics using either Au wire bonds or microwave probes. Electrical contact of the CPW ground planes with the Cu/Pd cap of the mesa was achieved using two large ($\sim 4 \times 2\,\mu m^2$) rectangular vias fabricated using photolithography and the same reactive ion etch used to fabricate the NC in the SiO_2.

The experimental setup for combined magnetoelectronic measurements and TRSKM with coherent injection locking is

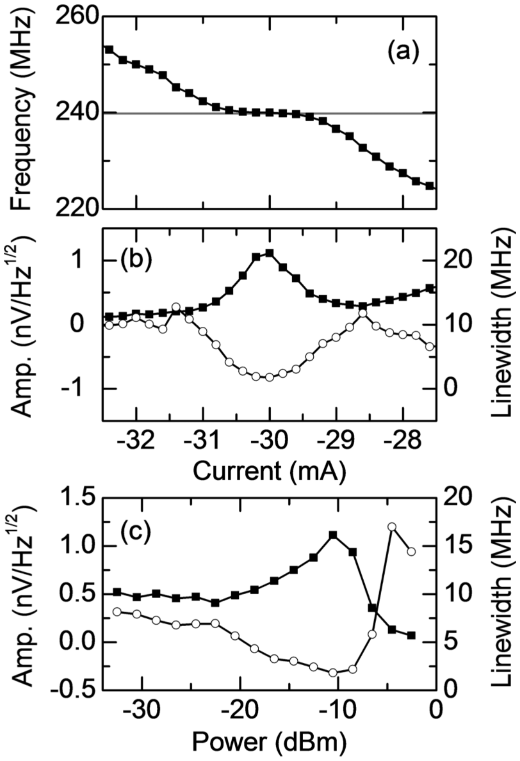

FIG. 2. (a) The STVO frequency as a function of dc current of device NC1 shows frequency locking at $f_{\mathrm{RF}}/2$ when $f_{\mathrm{RF}} = 480$ MHz. (b) The corresponding amplitude and linewidth reveal a maxima and minima close to the center of the locking range. (c) The amplitude and linewidth were found to be optimized when P_{RF} was ~ -10 dBm.

shown in Fig. 1(a). Measurements were performed on single NC devices with nominally identical NC diameter that were fabricated simultaneously on the same wafer. Three of seven operational devices (NC1, NC2, and NC3) were selected for this study due to the similarities exhibited in their free-running response, i.e., the response to a dc current only, Figs. 1(d)–1(f). Electrical measurements were performed by applying a dc current I_{dc} to the NC via the dc port of a bias tee. The RF emission of the STVO was detected via the ac port using a spectrum analyzer with a 10 dB preamplifier and a 100 kHz resolution bandwidth. A circulator was used to detect the RF emission of the STVO, while simultaneously applying an external RF current to the NC. The bandwidth of the circulator was 100 MHz (150 to 250 MHz), which was sufficient to observe the fundamental RF emission of the STVO.

To determine the optimum power P_{RF} of the RF current for injection locking, preliminary electrical measurements were performed on device NC1 [40]. Figure 2(a) shows frequency locking at 240 MHz around $I_{\mathrm{dc}} = -30$ mA for an injected RF current with $f_{\mathrm{RF}} = 480$ MHz and $P_{\mathrm{RF}} = -10$ dBm. As the dc current was swept, from immediately outside the locking range at $I_{\mathrm{dc}} = -31.4$ mA to the center of the locking range at $I_{\mathrm{dc}} = -30$ mA, an increase in amplitude (×5) and decrease in linewidth (×7) was observed, Fig. 2(b). At the center of the locking range ($I_{\mathrm{dc}} = -30$ mA), a sweep of P_{RF} from -30.5 to -0.5 dBm, revealed that the maximum amplitude and minimum linewidth were observed at approximately $P_{\mathrm{RF}} = -10$ dBm, for which the locking range was almost a maximum [41]. When $P_{\mathrm{RF}} < -30.5$ dBm no frequency locking was observed, while at $P_{\mathrm{RF}} = -0.5$ dBm the STVO signal was no longer observed. To recover the STVO microwave signal, it was necessary to once again nucleate gyrotropic auto-oscillations of the vortex core in the absence of an injected RF current. Unless otherwise stated, $P_{\mathrm{RF}} = -10$ dBm for all injection locking experiments. For values of f_{RF} that lay outside of the circulator bandwidth, the output power of the RF synthesizer was adjusted to compensate for transmission losses in the circulator to ensure that $P_{\mathrm{RF}} \sim -10$ dBm was injected through the NC for all values of f_{RF}.

For TRSKM measurements the microwave synthesizer was synchronized with the optical pulses of a femtosecond Ti:sapphire oscillator using the 10 and 80 MHz outputs of a low phase noise master clock, respectively. Therefore, it was necessary for the RF frequency to be an integer multiple m of the laser repetition rate ($m \times 80$ MHz) in order to acquire stroboscopic scanning Kerr images. For example, the schematic of the laser pulse train and the RF waveform in Fig. 1(a) correspond to $m = 2$. For electrical measurements, it was not necessary to restrict the RF frequency to integer multiples of the laser repetition rate.

TRSKM measurements were performed on device NC3 at a wavelength of 800 nm, at which the responsivity of the quadrant photodiodes of the polarizing bridge detector was approximately 90% of the optimal value of 6.5 A/W at ~920 nm. The probe beam was expanded ×5, linearly polarized, and focused to a diffraction limited spot onto the STVO mesa using a ×60 (0.85 numerical aperture) microscope objective lens. At a wavelength of 800 nm the spatial resolution was previously determined to be ~500 nm [42]. The quadrant photodiode, polarizing bridge detector was used to simultaneously detect two orthogonal in-plane components of the dynamic magnetization (ΔM_x and ΔM_y) using the longitudinal magneto-optical Kerr effect, in addition to the out-of-plane component (ΔM_z) using the polar Kerr effect. Time-resolved Kerr images were acquired at a fixed phase of the injected RF current by scanning the STVO mesa beneath the focused probe using a piezoelectric stage. Phase sensitive measurements were performed by phase modulating the RF current from 0° to 180° at ~3 kHz. Subsequently, vector-resolved Kerr signals, corresponding to ΔM_x, ΔM_y, and ΔM_z, were recovered at the modulation frequency using three lock-in amplifiers.

III. RESULTS AND DISCUSSION

A. Magnetoelectronic measurements

The free-running response of device NC2 to a dc current only is shown again in Fig. 3(a). As the magnitude of I_{dc} was increased from zero to 50 mA (not shown), the associated Oersted magnetic field curls the softer free-layer magnetization around the NC, which favors a vortex within the otherwise uniform free-layer magnetization. As the vortex is nucleated an antivortex is also generated and is understood to become pinned at defects within the free layer [43]. In zero applied magnetic field the onset of gyrotropic auto-oscillations of the vortex core was observed at $I_{\mathrm{dc}} = -21$ mA. As I_{dc} was swept from -50 to -10 mA the fundamental frequency, or

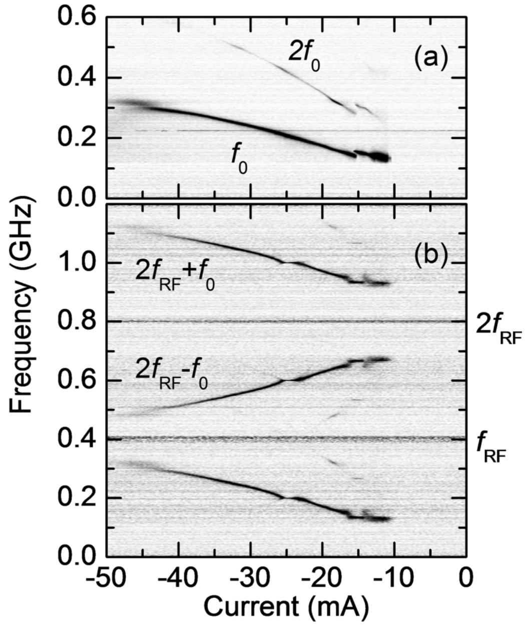

FIG. 3. (a) The free-running response of device NC2 to a dc current only. (b) SHIL exhibited in device NC2 subject to an injected RF current with $f_{\mathrm{RF}} = 400\,\mathrm{MHz}$. In (a) and (b) the white to black grayscale represents 0 to $1\,\mathrm{nV/Hz}^{1/2}$ and 0 to $0.5\,\mathrm{nV/Hz}^{1/2}$, respectively.

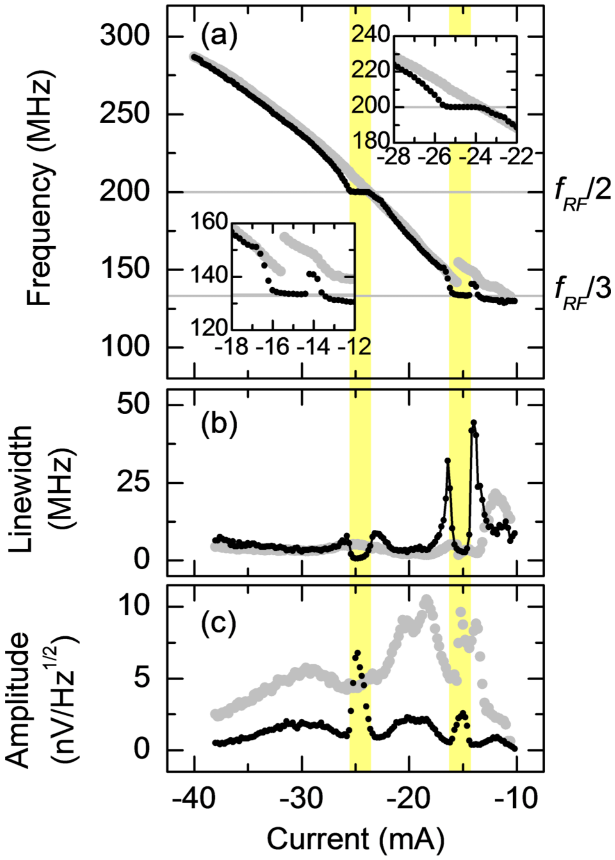

FIG. 4. (a) The free-running frequency response of device NC2 in response to the dc current only (gray filled symbols) and when exhibiting SHIL (black filled symbols) in response to an additional RF current with $f_{\mathrm{RF}} = 400\,\mathrm{MHz}$ (black filled symbols). The locking range at $f_{\mathrm{RF}}/2$ and $f_{\mathrm{RF}}/3$ are shown in more detail in the top-right and bottom-left insets, respectively. The linewidth (b) and amplitude (c) as a function of dc current for the free-running (gray filled symbols) and SHIL response (filled black symbols). In (a)–(c) the yellow bands correspond to the locking range.

first harmonic (f_0), of gyrotropic auto-oscillations decreases from ~300 to ~130 MHz, corresponding to more than one octave. A step transition in the frequency response can be seen around $I_{\mathrm{dc}} = -15\,\mathrm{mA}$. This is most likely due to a change in the core trajectory [44] as the equilibrium magnetization changes in response to the reducing amplitude of the Oersted field as the dc current approaches the "cut-off" threshold at $I_{\mathrm{dc}} = -10\,\mathrm{mA}$. The second harmonic ($2f_0$) can also be seen, but appears to be weaker than might be expected due to the limited bandwidth of the circulator.

When an RF current with $f_{\mathrm{RF}} = 400\,\mathrm{MHz}$ is injected, SHIL is observed, Fig. 3(b). Two ranges of dc current around $-25\,\mathrm{mA}$, and around $-15\,\mathrm{mA}$, exhibit frequency locking at $f_{\mathrm{RF}}/2$ and at $f_{\mathrm{RF}}/3$, respectively. Surprisingly, the frequency locking at $I_{\mathrm{dc}} = -15\,\mathrm{mA}$ ($f_{\mathrm{RF}}/3$) appears to stabilize the transition observed in the free-running response in Fig. 3(a). In addition to multiple locking ranges, nonlinear mixing (sum and difference signals) of the STVO fundamental response with the injected RF current leads to the presence of intermodulation modes [26]. The observed intermodulation modes in Fig. 3(b) have frequencies of $2f_{\mathrm{RF}} \pm f_0$ and therefore also show the signature of multiple frequency locking of the fundamental response.

Analysis of the RF emission reveals the expected increase in linewidth quality and enhanced amplitude in the locking range corresponding to $f_{\mathrm{RF}}/2$, Figs. 4(b) and 4(c), respectively. The response is similar to that observed in device NC1 [Fig. 2(b)], which demonstrates device-to-device consistency of the injection locking behavior. Figure 4(a) shows a direct comparison of the STVO fundamental frequency with and without an injected RF current with $f_{\mathrm{RF}} = 400\,\mathrm{MHz}$. As observed in Fig. 3(b), two frequency locking ranges are observed and shown in greater detail in the insets of Fig. 4(a). As the STVO frequency approaches the half-harmonic ($f_{\mathrm{RF}}/2$) of the injected RF current, frequency pulling [45] is observed [Fig. 4(a) and top-right inset], with a corresponding increase in linewidth and decrease in amplitude [Figs. 4(b) and 4(c), respectively]. When the STVO is locked at $f_{\mathrm{RF}}/2$, a reduction in the linewidth of approximately one order of magnitude (from 5.2 MHz to 570 kHz) is observed at $I_{\mathrm{dc}} = -24.8\,\mathrm{mA}$, while an increase in amplitude of approximately 60% from 4.3 to $6.8\,\mathrm{nV/Hz}^{1/2}$ is observed. A similar behavior of the linewidth and amplitude as a function of applied dc current is observed when the f_0 approaches $f_{\mathrm{RF}}/3$, albeit with enhanced linewidth to either side of the locking range. However, when f_0 is locked at $f_{\mathrm{RF}}/3$, the linewidth is approximately equal to that of the free-running STVO, while the amplitude is less than a third of the free-running value. While SHIL appears to stabilize the frequency around $I_{\mathrm{dc}} = -15\,\mathrm{mA}$, where a change in the equilibrium magnetic state may take place, the similarity of the locked and free-running linewidths at $f_{\mathrm{RF}}/3$ may suggest that there is significant disturbance to the vortex core trajectory (frequency via orbital radius, and phase via position on the

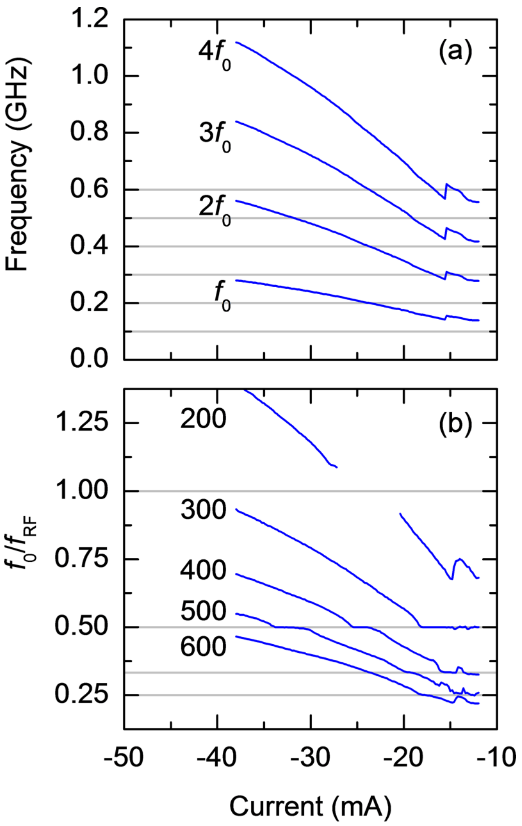

FIG. 5. (a) The free-running frequency response of device NC2 in response to the dc current only, and the calculated (i.e., nf_0) higher harmonics ($2f_0$, $3f_0$, $4f_0$), are shown (blue curves) overlaid with the frequencies of the injected RF current (gray curves). (b) SHIL of device NC2 by injecting an additional RF current with frequency in the range 200 to 600 MHz (value/MHz listed).

orbit) due to the competition between the change in the magnetic state and the onset of SHIL.

The effect of the RF frequency on the efficiency of SHIL was explored. The RF frequency was varied from 100 to 600 MHz in steps of 100 MHz. Subharmonic injection locking, where the RF frequency corresponds to a subharmonic of the STVO fundamental frequency ($f_{RF} = f_0/2$), has recently been reported in a nanopillar tunnel valve with vortices in the free and reference layers [20]. In our NC-STVO such frequency locking to an injected RF current with a frequency of 100 MHz was not observed. However, when $f_{RF} = f_0/2$ nonlinear mixing of the STVO fundamental response with the injected RF current was observed as a series of intermodulation modes with frequencies $2nf_{RF} \pm f_0$ ($n = 1,2,3,4,5$) [46].

In general, when the frequency of the RF current was equal to, or greater than, the STVO fundamental frequency, Fig. 5(a), injection locking was observed, Fig. 5(b). More specifically, locking was observed when the frequency of the injected RF current crossed either the fundamental frequency, or the frequency of a higher harmonic, with the latter resulting in SHIL. It can then be understood that subharmonic injection locking is not expected in our device since there is no subharmonic RF emission at half of the STVO fundamental frequency ($f_0/2$) [38].

When the fundamental frequency of the STVO was equal to that of the RF current ($f_0 = f_{RF}$), injection locking was observed around $I_{dc} = -23.6$ mA that corresponds to the f_0 crossover with f_{RF} at 200 MHz, Fig. 5(a). Such frequency locking at the fundamental frequency has previously been reported by a number of groups [20,32–35]. Since the amplitude of the residual RF signal was at least two orders of magnitude larger than that of the STVO emission, the latter could not be reliably extracted around the locking range and have therefore been omitted from Fig. 5(b). In this case only, the locking range was determined from the values of I_{dc} at which the STVO response vanished beneath the RF signal.

When $f_{RF} = 300$ MHz, locking to the fundamental response was not possible since the RF frequency was greater than the maximum fundamental frequency of the STVO, Fig. 5(a). However, Fig. 5(a) shows that the f_{RF} coincides with that of the second harmonic ($2f_0$) at $I_{dc} = -16.6$ mA, and again at $I_{dc} = -14.4$ mA. SHIL then gives rise to frequency locking of the fundamental response around the crossover current with the second harmonic. At larger values of f_{RF}, SHIL was also observed. At $I_{dc} = -23.7$ mA a crossover of $f_{RF} = 400$ MHz with the second harmonic takes place, while at $I_{dc} = -15$ mA a close approach of f_{RF} to the third harmonic ($3f_0$) is sufficient for SHIL of the fundamental response to be observed. When $f_{RF} = 500$ MHz two frequency locking events are again observed corresponding to a crossover with the second and third harmonics at $I_{dc} = -31.9$ mA and $I_{dc} = -19.1$ mA. Finally, when $f_{RF} = 600$ MHz, frequency locking was only observed at $I_{dc} = -16.7$ mA corresponding to a crossover of f_{RF} with the fourth harmonic ($4f_0$), while locking at $f_{RF}/3$ (crossover with the third harmonic at $I_{dc} = -23.8$ mA) was not observed. The observed locking ranges corresponding to SHIL are not centered on the crossover currents of the higher harmonics with the injected RF frequency, Figs. 5(a) and 5(b). Frequency pulling tends to shift the locking range to a slightly larger magnitude of I_{dc} than might be expected from the crossover values in Fig. 5(a).

Figure 5(b) demonstrates that a STVO can be used as an ILFD, for which fractional locking is observed at $f_{RF}/2$ over a wide range of dc current. Furthermore, by tuning the dc current it is possible to access multiple fractions of the RF frequency at $f_{RF}/2$ and $f_{RF}/3$ in the same STVO for a single value of f_{RF}. A finer step in the value of f_{RF} in device NC1 revealed evidence of fractional locking at $f_{RF}/2$, $f_{RF}/3$, and $f_{RF}/4$ between the onset and cut-off values of the dc current for $f_{RF} = 480$ MHz [40]. This is only possible in STVOs for which the fundamental frequency of vortex gyration exhibits multioctave tunability. In contrast STOs utilizing higher frequency magnetization precession [13] would require bandwidths in excess of 40 GHz in order to exhibit SHIL at 20 GHz corresponding to $f_{RF}/2$, while the suboctave tunability of such STOs would not permit frequency locking at $f_{RF}/3$ or $f_{RF}/4$.

Systems that exhibit SHIL are expected to show a reduced locking efficiency at higher harmonics [20]. To explore this further in our NC-STVO, the locking range, linewidth, and amplitude of each locking event observed in Fig. 5(b) was extracted and plotted as a function of the locking fraction f_0/f_{RF}, Fig. 6. The locking range was extracted from the derivative of the linewidth as a function of dc current for which the sharp reduction of the linewidth on approach to

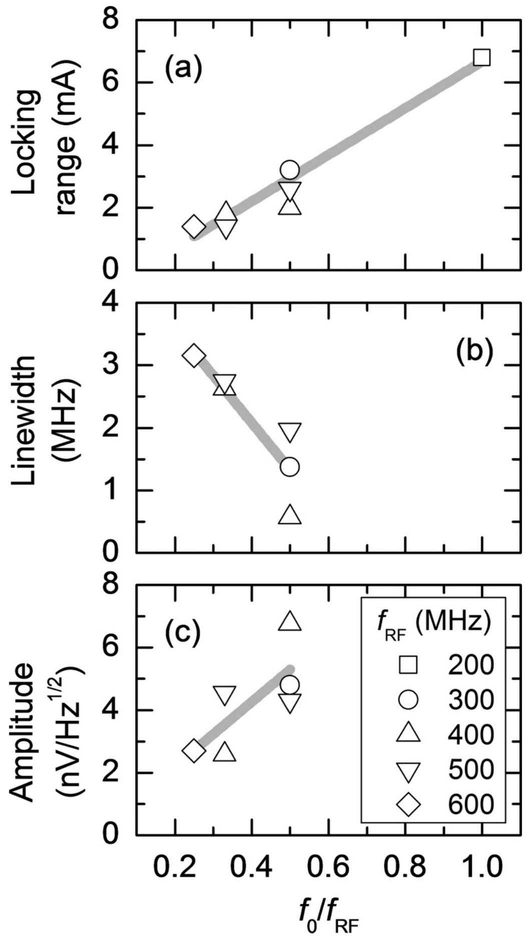

FIG. 6. (a) Extracted locking range as a function of locking fraction. (b) Minimum linewidth within each locking event as a function of locking fraction. (c) Maximum amplitude within each locking event as a function of locking fraction. The gray lines only serve as guides to the eye.

locking yields a peak in the derivative. The separation of the peaks was then taken as the locking range. One exception to this method was that used to extract the locking range when $f_{RF} = f_0$, for which the residual RF signal obscures the locked STVO emission, as described previously. In general there is an increase in locking range and amplitude as the locking fraction increases, which suggests that in general SHIL to the lower frequency harmonics is more efficient owing to their larger amplitude [20]. Similarly there is a general decrease in the linewidth as f_0/f_{RF} increases [Fig. 6(b)], again due to the enhanced efficiency of SHIL to the lower frequency harmonics. The efficiency of the nonlinear process of SHIL depends upon the amplitude of the higher harmonics, and therefore decreases as the harmonic number n increases [20,47]. In addition the linewidth of the higher harmonics of a free-running STVO has previously been shown to increase linearly as n increases [48]. The increased linewidth of the higher harmonics may play a crucial role in the SHIL process whereby the dispersion of frequency and/or phase may allow the STVO to more readily lock to the injected RF current [48]. In contrast, a sharply tuned nonlinear oscillator may not lock to an injected RF current, and so a minimum oscillator bandwidth may be required [45].

Deviations from these general trends were observed. For example, the locking range was not observed to vary monotonically as a function of the RF frequency. When $f_{RF} = 500$ and 300 MHz, the locking range at $f_{RF}/2$ was larger than that when $f_{RF} = 400$ MHz. The amplitude and linewidth of the free-running STVO emission may be responsible for these deviations. The linewidth is narrow at values of I_{dc} corresponding to $f_{RF}/2$ locking events for f_{RF} of 500 and 300 MHz, Fig. 4(b). At the same time, the amplitude of the free-running response was large in these regions, Fig. 4(b). On the other hand, when $f_{RF} = 600$ MHz no SHIL was observed at $f_{RF}/3$ despite f_{RF} crossing the third harmonic of the STVO at $I_{dc} = -23.8$ mA, Figs. 5(a) and 5(b). This may be due to a change in the gyrotropic trajectory as implied by the onset of a sharp increase in the amplitude at a similar value of I_{dc}, Fig. 4(b). As previously discussed the transitions in the core trajectory will take place as the Oersted field associated with the dc current reduces as the current is swept to the cut-off threshold. Corresponding changes in the symmetry of the trajectory as the dc current is reduced [44] may then lead to a variation in the efficiency of SHIL which then permits some locking events while others are more difficult to achieve.

B. Time-resolved scanning Kerr microscopy

While injection locking can be used to enhance the output power and phase stability of individual STVOs, phase locking of multiple STVOs can be achieved by injecting the same RF current, as demonstrated for a pair of tunnel valve nanopillar STVOs [33]. In NC-STVOs it is anticipated that the magnetization dynamics within magnetic layers shared by multiple oscillators can be used to achieve mutual synchronization resulting in enhanced output power and phase stability [25]. In addition to studying SHIL in electrical measurements, TRSKM was used to explore the differences in the magnetization dynamics generated by a single NC-STVO that is injection locked at its fundamental frequency f_0, and locked via the second harmonic ($2f_0$) using SHIL. To perform stroboscopic TRSKM measurements in these two locked states, it was necessary to set the frequency of the RF current to 160 and 320 MHz, respectively ($m = 2,4$), as described earlier.

TRSKM images acquired from device NC3 are shown in Fig. 7. The images represent the change in the dynamic magnetization due to the 180° phase modulation of the RF current while the STVO is phase locked. In TRSKM measurements a small in-plane bias magnetic field of ~5 mT was applied to ensure that the FL returned to the same equilibrium state necessary for successful stroboscopic scanning Kerr imaging. The applied field led to an increase in the nucleation current to a value of $I_{dc} = -28.1$ mA. When the fundamental frequency of the STVO was locked to an RF current with $f_{RF} = 160$ MHz and $P_{RF} \sim -13$ dBm, localized dynamics were observed. The dynamics extend outside of the perimeter of the center contact pad in the vicinity of the NC, as indicated by location A in the reflectivity image of Fig. 7(a). The observed dynamics have a complicated character [49]. The phase modulation of the RF current leads to the modulation of the vortex core position between two points on its trajectory that are separated by 180°. At a particular phase of the RF current, the observed dynamics are interpreted as the deflection of the magnetization

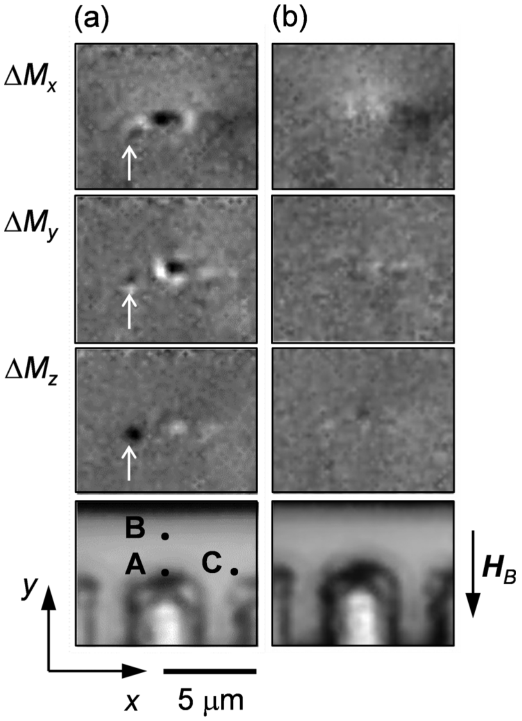

FIG. 7. (a) TRSKM images acquired from device NC3 corresponding to the change in three orthogonal components of the dynamic magnetization ΔM_x, ΔM_y, and ΔM_z for the case when the STVO is locked at $f_0 = f_{\mathrm{RF}}$ (a) and at $f_0 = f_{\mathrm{RF}}/2$ (b) using SHIL. The bottom image is a reflectivity image of the device. All four images in (a) and (b) were acquired simultaneously. In the Kerr images of ΔM_x and ΔM_y, the grayscale represents the change in magnetization where black and white represent $+M_S/2$ and $-M_S/2$, respectively.

between these two dynamic states [50]. When the STVO is instead locked using SHIL at $f_{\mathrm{RF}}/2 = 160\,\mathrm{MHz}$, where $f_{\mathrm{RF}} = 320\,\mathrm{MHz}$ and $P_{\mathrm{RF}} \sim -18\,\mathrm{dBm}$, the spatial character of the magnetization dynamics [Fig. 7(b)] reveal significant differences to that observed in Fig. 7(a). The strong contrast of the localized dynamics in Fig. 7(a) is no longer observed, however weaker contrast with a different spatial character is observed at location A [51]. This can be interpreted as a different trajectory, e.g., orbital radius, of the vortex gyration when phase locked at f_0 or $2f_0$. Despite the lower estimated RF power outside of the circulator bandwidth at 320 MHz, the amplitude of the dynamics far from the NC at location B in Figs. 7(a) and 7(b) appears to be similar. Kerr images acquired at $f_{\mathrm{RF}} = 160\,\mathrm{MHz}$ when $P_{\mathrm{RF}} \sim -13\,\mathrm{dBm}$ and $P_{\mathrm{RF}} \sim -18\,\mathrm{dBm}$ (not shown) do not show changes in the spatial character that are as marked as those in Fig. 7. Movies of the magnetization dynamics at 320 MHz do not reveal any dynamics in the extended film that oscillate at 160 MHz. Therefore, the locked STVO signal at $f_{\mathrm{RF}}/2 = 160\,\mathrm{MHz}$ is likely to correspond to vortex dynamics confined beneath the NC. Furthermore, the dynamic feature to the left of the center contact pad (indicated by white arrow) in Fig. 7(a), and apparent absence in Fig. 7(b), suggests that SHIL may also affect the equilibrium magnetization. The observed feature (arrow) in Fig. 7(a) is understood to be an antivortex that has moved further from the NC, but has been trapped by stray electromagnetic fields generated by the dc current in the CPW structure. Micromagnetic simulations have shown that the antivortex can move away from the NC and become pinned at the edge of the simulated mesh during the vortex-antivortex nucleation process [43]. In real devices it is expected that the antivortex would become pinned at a magnetic defect for example. However, for a particular bias field direction when injection locked at f_{RF}, the spatial character of the magnetization dynamics observed in TRSKM measurements was found to be unchanged even after the sample had been magnetized in different directions, injection locked at $f_{\mathrm{RF}}/2$, or cycled through a dc current hysteresis loop. Therefore, the reproducibility of the nucleation process and the equilibrium magnetization for a given device appear to be robust.

It should be noted that in Figs. 7(a) and 7(b) the phase of the RF current is similar and can be determined by the contrast of the dynamics observed far from the NC, which is observed to be closer to white in the positive y direction (location B), and closer to black in the positive x direction (location C). These “far-field” dynamics are the result of a small reorientation of the quasiuniform magnetization far from the NC due to the Oersted field associated with the RF current passing through the mesa and the CPW structure. When the dc current is reduced to zero (not shown), only the far field dynamics are observed (not shown), confirming that the localized dynamics are related to the spin-torque excitation by the dc current [49].

While the trajectory of the vortex core in a NC-STVO may be complicated by the quasiuniform equilibrium magnetization and the necessary presence of an antivortex within the FL, the trajectory can be considered in a simplified way for the case of SHIL. In a free-running NC-STVO, the vortex core can be assumed to occupy a concentric trajectory that is centered on the NC, while the Oersted field associated with the dc current acts as a concentric restoring potential that confines the core to its orbit [34]. When an RF current passes through the NC, an RF amplitude modulation of the current is introduced. While the modulation amplitude is typically an order of magnitude smaller than that of the dc current, the modulation of the Oersted field modulates the restoring potential. It can then be considered that the vortex core is periodically confined more tightly to the NC, or allowed to move further away. Figure 8 shows schematic illustrations of this interpretation. The frequency and phase noise associated with the vortex gyration allows its motion to phase lock to an RF Oe field that has frequency corresponding to the higher harmonics of the free-running response. This is shown for the first, second, third, and fourth harmonic in Figs. 8(a)–8(d), respectively, for which the trajectory of the free-running response is shown by the circular dotted line. The trajectory corresponding to $f_{\mathrm{RF}} = f_0$, $2f_0$, $3f_0$, and $4f_0$, in Figs. 8(a)–8(d), show 1, 2, 3, and 4 periods of enhanced and diminished confinement (radius of orbit) within a single orbit at the fundamental frequency. One should note that this interpretation is an oversimplification of a realistic NC-STVO. It does not take into account the nonuniform equilibrium magnetization, complicated core trajectories in the presence of bias magnetic fields and from interlayer coupling, and asymmetries in the current distribution. This is quite clear from the direct observation of the dynamics using TRSKM,

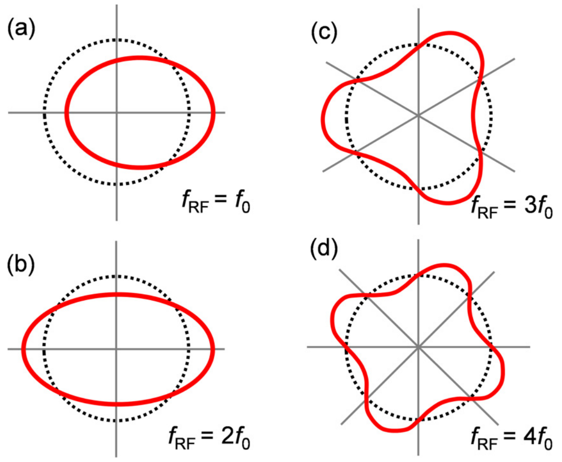

FIG. 8. Schematic illustration of the vortex core trajectory in the absence of an injected RF injected RF current (dotted circle), and in the presence of an RF current (solid red trajectory) with frequency equal to the first (a), second (b), third (c), and fourth (d) harmonic of the free-running orbit.

Fig. 7. In the simple framework of Fig. 8, one might expect to observe strong localized contrast in the vicinity of the NC in the Kerr images of Fig. 7(b). However, the Kerr images suggest that the dynamics in the immediate vicinity of the NC are very different for the case when the STVO is locked at f_0 and $2f_0$.

Micromagnetic simulations can reveal the sensitivity of the spatial character of the magnetization dynamics to these influences. Despite this sensitivity, in general the frequency response to a dc current is quite similar from device-to-device, for example see Figs. 1(d)–1(f). Small jumps, changes in gradient, and often splitting of the response may be signatures of device-to-device variations due to nanostructural inhomogeneity such as defects, surface roughness and coupling between layers, impurities, and grain orientation in the fixed layer [52]. These variations in the local magnetic environment may occur on length scales that are smaller than the NC diameter, but may have a similar effect on the gyration of a vortex to that of local defects [53]. Indeed, TRSKM images acquired from a fourth device that exhibited frequency spitting in its electrical response revealed a marked difference in the observed spatial character of the magnetization dynamics. While these measurements were not performed in sufficient detail to provide an informed discussion here, they do demonstrate that TRSKM is a powerful tool to study such device-to-device variations of NC-STVOs in relation to their electrical characteristics.

IV. SUMMARY

In summary, superharmonic injection locking has been observed in a NC-STVO. The nonlinear nature of the STVO allowed SHIL to be demonstrated up to (but not limited to) an injected RF frequency that was more than twice the maximum frequency of the free-running STVO. The SHIL locking events were shown to be located at values of the applied dc current that correspond to a crossover of the frequency of the injected RF current with that of the higher harmonics of the STVO. While there was a general correlation of the locking range, linewidth, and amplitude with the locking fraction, deviations from these trends were found to be related to variations in the linewidth and amplitude of the free-running response. TRSKM revealed that the spatial character of the magnetization dynamics in the vicinity of the NC was significantly different when the STVO was locked to an RF current with frequency corresponding to the first and second harmonics of the STVO. While the spatial character of the vortex core trajectory cannot be detected beneath the NC, a simplified interpretation of its gyration was presented. Specifically, a RF Oersted field, with frequency corresponding to one of the higher harmonics of the free-running STVO, can couple by perturbing the restoring potential experienced by the core. STVOs subject to SHIL may find future application as nanoscale injection locked frequency dividers. This work demonstrates that in a particular device, multiple locking fractions can be accessed for a particular RF frequency owing to the multioctave tunability of the STVO.

ACKNOWLEDGMENTS

The authors gratefully acknowledge the financial support of the United Kingdom Engineering and Physical Sciences Research Council under Grants EP/I038470/1 and EP/K008501/1, the Royal Society under Grant UF080837, the Swedish Research Council (VR), the Swedish Foundation for Strategic Research (SSF), and the Knut and Alice Wallenberg Foundation (KAW).

Open access to supporting research data is provided by Open Research Exeter [54].

---

[1] J. C. Slonczewski, J. Magn. Magn. Mater. **159**, L1 (1996).
[2] L. Berger, Phys. Rev. B **54**, 9353 (1996).
[3] M. Tsoi, A. G. M. Jansen, J. Bass, W. C. Chiang, M. Seck, V. Tsoi, and P. Wyder, Phys. Rev. Lett. **80**, 4281 (1998).
[4] J. A. Katine, F. J. Albert, R. A. Buhrman, E. B. Myers, and D. C. Ralph, Phys. Rev. Lett. **84**, 3149 (2000).
[5] T. J. Silva and W. H. Rippard, J. Magn. Magn. Mater. **320**, 1260 (2008).
[6] J. A. Katine and E. E. Fullerton, J. Magn. Magn. Mater. **320**, 1217 (2008).
[7] I. N. Krivorotov, N. C. Emley, J. C. Sankey, S. I. Kiselev, D. C. Ralph, and R. A. Buhrman, Science **307**, 228 (2005).
[8] S. I. Kiselev, J. C. Sankey, I. N. Krivorotov, N. C. Emley, R. J. Schoelkopf, R. A. Buhrman, and D. C. Ralph, Nature (London) **425**, 380 (2003).
[9] W. H. Rippard, M. R. Pufall, S. Kaka, S. E. Russek, and T. J. Silva, Phys. Rev. Lett. **92**, 027201 (2004).
[10] M. R. Pufall, W. H. Rippard, M. L. Schneider, and S. E. Russek, Phys. Rev. B **75**, 140404 (2007).
[11] S. Bonetti, P. Muduli, F. Mancoff, and J. Åkerman, Appl. Phys. Lett. **94**, 102507 (2009).
[12] Q. Mistral, M. van Kampen, G. Hrkac, J.-V. Kim, T. Devolder, P. Crozat, C. Chappert, L. Lagae, and T. Schrefl, Phys. Rev. Lett. **100**, 257201 (2008).

[13] S. Sani, J. Persson, S. M. Mohseni, Y. Pogoryelov, P. K. Muduli, A. Eklund, G. Malm, M. Käll, A. Dmitriev, and J. Åkerman, Nat. Commun. **4**, 2731 (2013).

[14] M. Manfrini, T. Devolder, J.-V. Kim, P. Crozat, C. Chappert, W. Van Roy, and L. Lagae, J. Appl. Phys. **109**, 083940 (2011).

[15] M. W. Keller, A. B. Kos, T. J. Silva, W. H. Rippard, and M. R. Pufall, Appl. Phys. Lett. **94**, 193105 (2009).

[16] B. Georges, J. Grollier, V. Cros, A. Fert, A. Fukushima, H. Kubota, K. Yakushijin, S. Yuasa, and K. Ando, Phys. Rev. B **80**, 060404 (2009).

[17] M. W. Keller, M. R. Pufall, W. H. Rippard, and T. J. Silva, Phys. Rev. B **82**, 054416 (2010).

[18] M. Quinsat, D. Gusakova, J. F. Sierra, J. P. Michel, D. Houssameddine, B. Delaet, M. C. Cyrille, U. Ebels, B. Dieny, L. D. Buda-Prejbeanu, J. A. Katine, D. Mauri, A. Zeltser, M. Prigent, J. C. Nallatamby, and R. Sommet, Appl. Phys. Lett. **97**, 182507 (2010).

[19] E. Grimaldi, A. Dussaux, P. Bortolotti, J. Grollier, G. Pillet, A. Fukushima, H. Kubota, K. Yakushiji, S. Yuasa, and V. Cros, Phys. Rev. B **89**, 104404 (2014).

[20] R. Lebrun, A. Jenkins, A. Dussaux, N. Locatelli, S. Tsunegi, E. Grimaldi, H. Kubota, P. Bortolotti, K. Yakushiji, J. Grollier, A. Fukushima, S. Yuasa, and V. Cros, Phys. Rev. Lett. **115**, 017201 (2015).

[21] S. Kaka, M. R. Pufall, W. H. Rippard, T. J. Silva, S. E. Russek, and J. A. Katine, Nature (London) **437**, 389 (2005).

[22] F. B. Mancoff, N. D. Rizzo, B. N. Engel, and S. Tehrani, Nature (London) **437**, 393 (2005).

[23] A. N. Slavin and V. S. Tiberkevich, Phys. Rev. B **74**, 104401 (2006).

[24] X. Chen and R. H. Victora, Phys. Rev. B **79**, 180402 (2009).

[25] A. Ruotolo, V. Cros, B. Georges, A. Dussaux, J. Grollier, C. Deranlot, R. Guillemet, K. Bouzehouane, S. Fusil, and A. Fert, Nat. Nanotechnol. **4**, 528 (2009).

[26] P. K. Muduli, Y. Pogoryelov, Y. Zhou, F. Mancoff, and J. Åkerman, Integrated Ferroelectrics **125**, 147 (2011).

[27] A. D. Belanovsky, N. Locatelli, P. N. Skirdkov, F. A. Araujo, J. Grollier, K. A. Zvezdin, V. Cros, and A. K. Zvezdin, Phys. Rev. B **85**, 100409 (2012).

[28] A. D. Belanovsky, N. Locatelli, P. N. Skirdkov, F. Abreu Araujo, K. A. Zvezdin, J. Grollier, V. Cros, and A. K. Zvezdin, Appl. Phys. Lett. **103**, 122405 (2013).

[29] N. Locatelli, A. Hamadeh, F. Abreu Araujo, A. D. Belanovsky, P. N. Skirdkov, R. Lebrun, V. V. Naletov, K. A. Zvezdin, M. Muñoz, J. Grollier, O. Klein, V. Cros, and G. de Loubens, Sci. Rep. **5**, 17039 (2015).

[30] A. Houshang, E. Iacocca, P. Dürrenfeld, S. R. Sani, J. Åkerman, and R. K. Dumas, Nat. Nano **11**, 280 (2016).

[31] S. Urazhdin, P. Tabor, V. Tiberkevich, and A. Slavin, Phys. Rev. Lett. **105**, 104101 (2010).

[32] R. Lehndorff, D. E. Bürgler, C. M. Schneider, and Z. Celinski, Appl. Phys. Lett. **97**, 142503 (2010).

[33] A. Dussaux, A. V. Khvalkovskiy, J. Grollier, V. Cros, A. Fukushima, M. Konoto, H. Kubota, K. Yakushiji, S. Yuasa, K. Ando, and A. Fert, Appl. Phys. Lett. **98**, 132506 (2011).

[34] S. Y. Martin, N. de Mestier, C. Thirion, C. Hoarau, Y. Conraux, C. Baraduc, and B. Diény, Phys. Rev. B **84**, 144434 (2011).

[35] P. Bortolotti, E. Grimaldi, A. Dussaux, J. Grollier, V. Cros, C. Serpico, K. Yakushiji, A. Fukushima, H. Kubota, R. Matsumoto, and S. Yuasa, Phys. Rev. B **88**, 174417 (2013).

[36] N. Locatelli, A. Mizrahi, A. Accioly, R. Matsumoto, A. Fukushima, H. Kubota, S. Yuasa, V. Cros, L. G. Pereira, D. Querlioz, J. V. Kim, and J. Grollier, Phys. Rev. Appl. **2**, 034009 (2014).

[37] A. Slavin and V. Tiberkevich, IEEE Trans. Magn. **45**, 1875 (2009).

[38] H. R. Rategh and T. H. Lee, IEEE J. Solid-State Circuits **34**, 813 (1999).

[39] H. R. Rategh and T. H. Lee, presented at the VLSI Circuits, 1998. Digest of Technical Papers. 1998 Symposium on, 1998 (unpublished).

[40] See Supplemental Material at http://link.aps.org/supplemental/10.1103/PhysRevB.94.094404 for the current-frequency spectral maps of SHIL in device NC1 when subject to an applied RF current with frequency of 480 MHz.

[41] See Supplemental Material at http://link.aps.org/supplemental/10.1103/PhysRevB.94.094404 for movie "RF_Power.mp4" that shows the RF power dependence of injection locking in device NC1.

[42] P. S. Keatley, P. Gangmei, M. Dvornik, R. J. Hicken, J. Grollier, C. Ulysse, J. R. Childress, and J. A. Katine, in *Magnonics*, edited by S. O. Demokritov and A. N. Slavin (Springer, Berlin, 2013), Vol. 125, p. 17.

[43] S. Petit-Watelot, J.-V. Kim, A. Ruotolo, R. M. Otxoa, K. Bouzehouane, J. Grollier, A. Vansteenkiste, B. Van de Wiele, V. Cros, and T. Devolder, Nat. Phys. **8**, 682 (2012).

[44] G. Hrkac, P. S. Keatley, M. T. Bryan, and K. Butler, J. Phys. D. **48**, 453001 (2015).

[45] R. Adler, Proc. IRE **34**, 351 (1946).

[46] See Supplemental Material at http://link.aps.org/supplemental/10.1103/PhysRevB.94.094404 for the current-frequency spectral maps acquired for different values of the RF frequency.

[47] I. Schmideg, Proc. IEEE **59**, 1250 (1971).

[48] F. Sanches, V. Tiberkevich, K. Y. Guslienko, J. Sinha, M. Hayashi, O. Prokopenko, and A. N. Slavin, Phys. Rev. B **89**, 140410 (2014).

[49] See Supplemental Material at http://link.aps.org/supplemental/10.1103/PhysRevB.94.094404 for time-resolved Kerr movie "TRSKM_160MHz.mp4" showing magnetization dynamics when the RF frequency is equal to that of the first harmonic of the STVO.

[50] P. S. Keatley, S. R. Sani, G. Hrkac, S. M. Mohseni, P. Dürrenfeld, T. H. J. Loughran, J. Åkerman, and R. J. Hicken, Phys. Rev. B **94**, 060402(R) (2016).

[51] See Supplemental Material at http://link.aps.org/supplemental/10.1103/PhysRevB.94.094404 for time-resolved Kerr movie "TRSKM_320MHz.mp4" showing magnetization dynamics when the RF frequency is equal to that of the second harmonic of the STVO.

[52] S. Tamaru and D. S. Ricketts, IEEE Magn. Lett. **3**, 3000504 (2012).

[53] R. L. Compton and P. A. Crowell, Phys. Rev. Lett. **97**, 137202 (2006).

[54] http://hdl.handle.net/10871/23168.